Title

Antisense therapy in a rat model of Alexander disease reverses GFAP pathology, white matter deficits, and motor impairment

Journal

Science Translational Medicine, 13(620)

ISSN

1946-6234

Authors

Hagemann, Tracy L
Powers, Berit
Lin, Ni-Hsuan
et al.

Publication Date

2021-11-17

DOI

10.1126/scitranslmed.abg4711

Peer reviewed

HHS Public Access

Author manuscript

Sci Transl Med. Author manuscript; available in PMC 2022 May 17.

Published in final edited form as:

Sci Transl Med. 2021 November 17; 13(620): eabg4711. doi:10.1126/scitranslmed.abg4711.

Antisense therapy in a rat model of Alexander disease reverses GFAP pathology, white matter deficits, and motor impairment**

Tracy L. Hagemann[1,*], **Berit Powers**[2], **Ni-Hsuan Lin**[3], **Ahmed F. Mohamed**[1], **Katerina L. Dague**[1,†], **Seth C. Hannah**[1,‡], **Gemma Bachmann**[2], **Curt Mazur**[2], **Frank Rigo**[2], **Abby L. Olsen**[4], **Mel B. Feany**[5], **Ming-Der Perng**[3], **Robert F. Berman**[6], **Albee Messing**[1,7]

[1]Waisman Center, University of Wisconsin-Madison, Madison, WI 53705, USA

[2]Ionis Pharmaceuticals, Carlsbad, CA 92010, USA

[3]Institute of Molecular Medicine, College of Life Sciences, National Tsing Hua University, Hsinchu 30013, Taiwan

[4]Department of Neurology, Brigham and Women's Hospital, Harvard Medical School, Boston, MA 02115, USA

[5]Department of Pathology, Brigham and Women's Hospital, Harvard Medical School, Boston, MA 02115, USA

[6]Department of Neurological Surgery and M.I.N.D Institute, University of California, Davis, Davis, CA 95616, USA

[7]Department of Comparative Biosciences, School of Veterinary Medicine, University of Wisconsin-Madison, Madison, WI 53705, USA

Abstract

*To whom correspondence should be addressed: tlhagemann@wisc.edu.

†Present address: Department of Surgery and Simmons Comprehensive Cancer Center, UT Southwestern Medical Center, Dallas, TX 75235, USA

‡Present address: Department of Animal and Avian Sciences, University of Maryland, College Park, MD 20742, USA

Author contributions: T.L.H, B.P., C.M., F.R., M.B.F., M.-D.P, R.F.B., and A.M designed the study and participated in preparation of the manuscript, A.L.O. analyzed data and participated in preparation of the manuscript, T.L.H and A.F.M. performed initial RNA and protein analysis and immunohistochemistry to validate the model, N.-H.L. and M.-D.P. prepared protein for all other immunoblot analysis of astrocyte proteins, K.L.D performed myelin protein analysis, other immunoblotting in ASO treated animals, and immunohistochemistry, G.B. performed ICV injections, tissue collection and RNA analysis for ASO treated animals, S.C.H. prepared protein lysates and fractions and performed ELISA assays for GFAP and rat IgG. T.L.H., S.C.H., and A.M analyzed EM micrographs for g-ratio determination.

Competing interests: B.P., C.M., G.B., and F.R. receive salaries from and are shareholders in Ionis Pharmaceuticals. A.M. was a consultant for Symbiotix. T.L.H., N.-H.L., A.F.M., K.L.D., S.C.H., A.L.O., M.B.F., M.-D.P, and R.F.B. have no competing interests.

Supplementary Materials
Materials and Methods
Figs. S1 to S14
Tables S1 to S2
Movies S1 to S7
Data file S1
References (67–75)

Alexander disease (AxD) is a devastating leukodystrophy caused by gain-of-function mutations in *GFAP*, and the only available treatments are supportive. Recent advances in antisense oligonucleotide (ASO) therapy have demonstrated that transcript targeting can be a successful strategy for human neurodegenerative diseases amenable to this approach. We have previously used mouse models of AxD to show that *Gfap*-targeted ASO suppresses protein accumulation and reverses pathology; however, the mice have a mild phenotype with no apparent leukodystrophy or overt clinical features and are therefore limited for assessing functional outcomes. In this report, we introduce a rat model of AxD that exhibits hallmark pathology with GFAP aggregation in the form of Rosenthal fibers, widespread astrogliosis, and white matter deficits. These animals develop normally during the first postnatal weeks but fail to thrive after weaning and develop severe motor deficits as they mature, with about 14% dying of unknown cause between 6 and 12 weeks of age. In this model, a single treatment with *Gfap*-targeted ASO provides long-lasting suppression, reverses GFAP pathology, and, depending on age of treatment, prevents or mitigates white matter deficits and motor impairment. In this report, we characterize an improved animal model of AxD with myelin pathology and motor impairment, recapitulating prominent features of the human disease, and use this model to show that ASO therapy has the potential to not only prevent but also reverse many aspects of disease.

INTRODUCTION

Alexander disease (AxD) is a rare neurogenetic disorder caused by dominant mutations in the gene encoding glial fibrillary acidic protein (*GFAP*), the major intermediate filament protein of astrocytes in the central nervous system (CNS) (1). Age of onset ranges from infancy through adulthood, and symptoms include deficits in motor, cognitive, and brain stem functions, failure to thrive, and seizures. In most cases, the disease is progressive and fatal (2). The pathological hallmark of all forms of AxD is the presence of astrocyte inclusion bodies known as Rosenthal fibers (RFs). Whether these protein aggregates are themselves toxic is not yet known. Nevertheless, what begins as primary dysfunction of astrocytes leads to a cascade of effects involving virtually every other cell type of the CNS (3, 4). AxD has therefore become a unique model for primary astrocytopathy, with the potential to inform our understanding of astrocyte dysfunction in many neurological diseases.

Because AxD is a monogenic gain-of-function disease, suppression of GFAP expression has recently emerged as the most promising therapeutic strategy (5, 6). In mouse models engineered to carry *Gfap* point mutations mimicking disease-associated variants in humans, single intracerebroventricular (ICV) injections of *Gfap*-targeted antisense oligonucleotides (ASOs) reduced brain and spinal cord GFAP transcript and protein to nearly undetectable amounts and reversed key aspects of cellular and molecular pathology (7). However, the existing mouse models are not ideal. Although they display several features of the human disease, such as RFs, astrogliosis, and increased seizure susceptibility, they have no motor deficits, no evident leukodystrophy, and only subtle and strain-dependent deficits in cognition (8, 9). Hence, the ability to fully evaluate the risks and benefits of GFAP suppression on clinically relevant phenotypes is limited.

Here, we report a translationally relevant rat model of AxD that displays more extensive pathology, including more severe behavioral symptoms and abnormalities of white matter. We find that administration of *Gfap*-targeted ASOs to these rats can prevent or reverse much of the pathology and symptoms, even when given at the peak manifestation of disease. These results offer promise for the development of ASOs as an effective treatment strategy for an otherwise progressive and devastating disease.

RESULTS

Validation and phenotyping of GFAP mutant rat model

To generate a rat model of AxD, we used CRISPR-Cas9 mutagenesis to reproduce the severe R239H mutation observed solely in patients with early-onset AxD at the orthologous GFAP-Arg237 position in the rat (Fig. 1A). Screening of founder animals led to the generation of two separate lines: one with the desired R237H mutation, and a second with a single nucleotide deletion upstream of the targeted sequence, generating a frameshift and premature stop codon (fig. S1). Sequence analysis of cloned complementary DNAs from rat brain in the R237H line demonstrates an intact full-length transcript from the targeted allele. Similar to patients with the disease and our mouse models (9, 10), expression of the R237H variant causes a spontaneous increase in *Gfap* transcript (Fig 1B, left). In the second rat line, the deletion essentially creates a GFAP knockout rat with reduced transcript (Fig. 1B, right) and no detectable GFAP protein (Fig. 1C, right). We used this knockout line to cross with R237H rats to confirm protein expression from the targeted R237H allele (Fig. 1C, left). Immunoblotting with either a monoclonal antibody recognizing the GFAP tail domain or a polyclonal antibody demonstrates expression of the full-length 50-kD protein. The production of a GFAP null line provides a useful control, but similar to genetic knockout in the mouse (11–14), loss of GFAP function in the rat has no overt effects. Because AxD-associated point mutations lead to a toxic gain of function for the encoded protein (5), we focus here on the heterozygous point mutant R237H rat.

R237H rats meet normal developmental milestones (Fig. 1D) and are physically difficult to distinguish from their wild-type littermates during the first three postnatal weeks. However, after weaning, both males and females fail to thrive and by 8 weeks are gaunt, with virtually no white fat (fig. S2) and reduced organ size (Fig. 1, E to G), although brain is relatively spared. At this stage, R237H rats are frail with a severely hunched posture, global paucity of movement, and severe gait impairment in which the hind paws frequently splay out laterally and posteriorly. These progressive changes are demonstrated by open field activity where weanlings show no difference between genotypes, but the same animals at 8 weeks show marked reduction in activity (Fig 1H). Reduced strength, deficits in coordination, and gait abnormalities, are further exemplified in adult R237H rats by forelimb grip measures, rotarod performance, and paw placement on a horizontal ladder (Fig. 1I, and movies S1 and S2). At 8-weeks, they struggle to stay on the rotarod even at low speeds, and on the ladder test, exhibit impaired ability to grasp the rungs using both the front and hind paws, with frequent slips. Although genotype and sex ratios are normal at weaning (R237H: 24.4% male, 24.8% female; wildtype: 24.6% male, 26.2% female; n=1,428), approximately 14% of AxD rats die between 6 and 12 weeks (including 5.5% found moribund or with severe hemi/

paraparesis or paralysis and euthanized for humane reasons) (Fig. 1J). Occasional surviving rats develop forelimb monoplegia between 6 and 8 weeks of age.

GFAP accumulation, RFs, and astrogliosis in R237H rats

GFAP mutations in AxD lead to GFAP accumulation, protein aggregation in the form of RFs, and astrogliosis. To determine whether R237H rats replicate key pathologic features of human disease, we first assessed GFAP expression and protein aggregation as the animals mature. By 3 weeks of age, brain GFAP is significantly ($P<0.01$) increased and by 8 weeks markedly elevated (Fig. 2A and fig. S3A). In mutant animals, lower molecular weight fragments are also apparent with immunoblotting and most likely reflect 24 and 26 kD caspase-6 cleavage products (15, 16). An accumulation of high molecular weight ubiquitinated proteins is also apparent (Fig. 2B and fig. S3B), suggesting diminished proteasome capacity. Further analysis of RF-associated proteins shows an increase in small heat shock proteins Hsp27 (HSPB1) and αB-crystallin (CRYAB), autophagy cargo protein sequestosome (p62, SQSTM1), intermediate filament vimentin (VIM), and a more recently identified component, cyclinD2 (CCND2; Fig. 2B and fig. S3B) (17–20).

In mouse models of AxD, astrocyte pathology is localized and more prominent in forebrain structures, with limited pathology in hindbrain (9). GFAP expression in the adult R237H rat is markedly elevated, at both the transcript and protein level, in all regions analyzed including brainstem, cerebellum, hippocampus, cortex and corpus callosum, with the exception of spinal cord (which begins with the highest basal expression) (Fig. 2C; 8 weeks of age). Although an inadequate response by the ubiquitin-proteasome system likely exacerbates protein accumulation, increased GFAP in AxD is also driven by transcription (7, 21, 22). Western blot analysis of subcellular protein fractions indicates activation of both signal transducer and activator of transcription (STAT3) and nuclear factor κB (NFκB), transcription factors known to regulate *Gfap*, as evidenced by elevation of both native and phosphorylated forms of the two, and localization of phosphorylated proteins in the nuclear compartment (Fig. 2D and fig. S4, A and B). Immunofluorescence labeling confirms nuclear localization of phosphorylated STAT3 in GFAP positive astrocytes and potentially other cell types (fig. S4C to E). Note that the nuclear membrane intermediate filament lamin A/C, used in these experiments to confirm enrichment of nuclear proteins (Fig. 2D), is also elevated in the R237H rat. These results agree with our previous report showing elevation of A-type lamin in both animal models and patients with AxD, implicating mechanotransduction signaling in AxD pathogenesis (23). GFAP in cerebrospinal fluid (CSF) and plasma also increases as AxD rats mature, with significant elevation by 8 weeks of age ($P<0.0001$), when accumulation in brain is maximal and animals are severely affected (Fig. 2E). Elevation of GFAP in these two body fluid compartments may provide useful biomarkers for therapeutic testing in the model.

Hypertrophic reactive astrocytes (24) are apparent throughout the R237H rat CNS and have abnormal morphology with protein aggregates and thick blunted processes (Fig. 2F and fig. S5). RFs are evident by light microscopy as early as postnatal day 14 (P14) and are prominent as both large aggregates and smaller puncta in brain and spinal cord of young adult animals (Fig. 2G and fig. S6). Electron microscopy demonstrates classic RFs

as observed in astrocytes of patients with AxD: dense osmiophilic aggregates enmeshed in swirls of intermediate filaments (Fig. 2H).

Astrocyte stress response in R237H rats: Pathology and function

Although cellular GFAP is predominantly filamentous, the protein normally exists in equilibrium between a detergent-soluble pool of monomers, dimers, and tetramers and an insoluble pool of unit length and full filaments. Biochemically, RFs in AxD are even less soluble and can be partitioned further from the filaments (20). In R237H rats, total GFAP protein is elevated throughout the brain, but in spinal cord, where GFAP expression is normally high, no further elevation is observed (Fig. 2C). To determine whether GFAP aggregates have similar properties in the R237H rat and whether brain and spinal cord show differences in these pools, we separated protein lysates from hippocampus and cervical cord into soluble, cytoskeletal, and RF-enriched fractions (20). In hippocampus, GFAP was elevated in both the cytoskeletal and RF fractions (Fig. 3A and fig. S7A), whereas in spinal cord GFAP showed little change in the cytoskeletal fraction, but a marked increase in the RF fraction (Fig. 3B and fig. S7B). These data show that the presence of mutant GFAP by itself, independent of GFAP elevation, in the spinal cord is sufficient to produce AxD-associated pathology.

We also analyzed AxD-associated stress response proteins. SQSTM1 displayed a pattern similar to GFAP in both CNS regions, but other stress proteins varied in elevation and cellular compartment (Fig. 3, A and B, and fig. S7, A and B). HSPB1 was elevated in all fractions in both regions, whereas CRYAB was not detectable in the RF fraction, at either the expected molecular weight or as a higher molecular mass species, and may have been dissociated from RFs by urea solubilization of the cytoskeletal fraction. Similar results were observed in a previous study using our mouse models of AxD where 80% of CRYAB was detected in the urea soluble cytoskeletal fraction (20). CCND2 was predominantly detected in the RF fraction. Note that most cytoplasmic proteins are extracted in the soluble fraction, including glyceraldehyde-3-phosphate dehydrogenase (GAPDH). Histologically, immunofluorescence labeling of SQSTM1 showed colocalization with GFAP and provides a robust marker for GFAP protein aggregation (Fig. 3, C and D, and fig S8A). CRYAB, which is normally primarily expressed in oligodendrocytes, is elevated in R237H rat astrocytes and appears to colocalize with GFAP (Fig. 3, E to G, and fig S8B). Ubiquitin labeling was prevalent in astrocytes, but did not always colocalize with GFAP, which may reflect accumulation of other ubiquitinated proteins (Fig. 3H and fig. S8C).

Prior studies of astrocyte response to injury and disease, including AxD, have implicated caspase-3 activation (25, 26). To evaluate astrocyte injury, we examined whether cleaved caspase-3 was present in the R237H rat. We found prominent caspase-3 activation apparent in hippocampus, corpus callosum, and other regions of the CNS as early as 3-weeks of age when the overall clinical presentation is still relatively mild (figs. S8D and S9). Co-labeling with markers for astrocytes (Sox9 and GFAP), oligodendrocytes (Olig2), and neurons (NeuN) in adult animals showed that cleaved caspase-3 was specifically localized to astrocytes (Fig. 3, I to N, and fig S8D). Further analysis with TUNEL (terminal deoxynucleotide transferase-mediated deoxyuridine triphosphate nick end

labeling) identified a small population of apoptotic cells in R237H rats. Not all positive cells could be identified as astrocytes, and TUNEL positive cells were also apparent in wild-type animals (fig. S9D). Caspase-3 activation has been associated with reactive astrocytes in other injury models, particularly in rats, and may have non-apoptotic functions such as cytoskeletal rearrangement (27–31).

To evaluate potential effects of GFAP induced pathology on astrocyte function, we analyzed the glutamate transporter GLT-1 (SLC1A2), the major gap junction protein in astrocytes, connexin 43 (GJA1), water channel aquaporin 4 (AQP4), and potassium channel Kir4.1 (KCNJ10). R237H rats show a marked loss of SLC1A2 by 8 weeks of age as shown by immunoblotting of membrane fractions from different brain regions and spinal cord (Fig. 4A and fig. S10A), consistent with reductions observed in mouse models and patients with AxD (32). Previous studies with in vitro models have also suggested a lack of gap junction connectivity in astrocytes expressing mutant GFAP (32). Immunofluorescence labeling of GJA1 in hippocampus shows prominent expression in the hilus and near the fissure vasculature in wild-type animals, but patchy labeling with more puncta located away from vessels in R237H rats (Fig. 4, B and C, and fig. S10, B and C). In spinal cord GJA1 expression is generally reduced (Fig. 4, D and E, and fig. S10D), and membrane tissue fractions show decreased GJA1 in all regions analyzed (Fig. 4A and fig. S10A). AQP4 distribution also appears to be altered and depolarized away from astrocyte endfeet in hippocampus, and overall staining intensity is reduced in spinal cord (Fig. 4, F to I, and fig S10, E to G). Protein quantitation via immunoblotting shows a similar pattern with no change in hippocampus and corpus callosum and reductions in brainstem and spinal cord (Fig 4A and fig. S10A). KCNJ10, which tends to distribute in the same subcellular compartments as AQP4 (33), is localized to astrocyte somata in hippocampus and virtually absent in spinal cord (Fig. 4, A, J to M, and fig. S10A and H to J). AQP4, KCNJ10, and GJA1 normally localize to astrocyte endfeet and regulate ion and water transport. To determine whether edema may contribute to CNS pathology in the R237H rat, we measured water content in different brain regions and spinal cord. With the exception of cerebellum, we found increases in all regions tested (Fig. 4N), with the most marked changes occurring in areas predominantly composed of white matter including spinal cord, brainstem and corpus callosum. A small but significant decrease was observed in cerebellum (P=0.00094). To assess blood brain barrier integrity, we measured immunoglobulin G (IgG) content in hippocampus and spinal cord and found modest elevation in hippocampus (Fig. 4O).

Non-cell-autonomous effects of mutant GFAP and astrocyte dysfunction

Given the molecular and morphological changes in AxD astrocytes and the activation of neuroinflammatory pathways, we wanted to survey how these changes affect other cell types in the R237H rat CNS. Iba1 immunolabeling shows an increase in hypertrophic microglia in most regions of the CNS (fig. S11, A and B). In areas such as cortex and spinal cord gray matter (Fig. 5, A to E), microglia appear to wrap around GFAP-laden astrocytes (Fig. 5, B and E), with some having a reactive ameboid morphology (Fig. 5D and fig. S11B). Oligodendrocyte precursor cells show an increase in NG2 immunolabeling particularly in white matter (Fig. 5, F and G, and fig. S11C), suggesting this glial population is also responding to astrocyte pathology. Identification of mature oligodendrocytes with

adenomatus polyposis coli (APC, monoclonal CC-1 antibody) or glutathione S-transferase (GST)-π was unfortunately hampered by cross reactivity with reactive astrocytes (34–36).

Within the dense collection of reactive glia, neurons show signs of degeneration and loss. In hippocampus, both the pyramidal and the dentate granule cell layers appear mottled and thinned, suggesting a reduced neuronal population (Fig. 5, H and I, and fig. S11D). We have previously reported that GFAP mutations lead to deficits in adult neurogenesis in mouse models of AxD (8), and R237H rats have virtually no doublecortin positive neurons in the dentate gyrus at 8-weeks of age (Fig. 5, J and K, and fig. S11E). Whether the lack of new neurons is the result of deficits in the adult radial glia-like stem cells, which express GFAP, or a reactive subgranular zone niche remains to be determined. In spinal cord, electron microscopy shows enlarged bulbous neurites adjacent to motor neurons in the ventral horn (Fig. 5L and fig. S11F), some of which show evidence of degeneration with collections of membranous debris and vacuolized mitochondria (Fig. 5M).

Myelin deficits in R237H rat model of AxD

AxD is classically characterized as a leukodystrophy; nevertheless, little is known regarding how a primary disorder of astrocytes leads to deficits in white matter and myelination. R237H rats have noticeably smaller spinal cords compared with wild-type littermates, and area measures from cross-sections of the cervical cord enlargement (C5) reflect this size difference (Fig. 6A). However, separate measures of white and gray matter show a disproportionate reduction in white matter (Fig. 6A). To assess further whether R237H rats have myelin deficits, we focused on spinal cord as a severely affected CNS region. Immunoblotting for myelin proteins shows that both MBP (myelin basic protein) and CNP (a2',3'-cyclic nucleotide 3' phosphodiesterase) are modestly but significantly reduced in R237H rats at 8 weeks of age ($P<0.001$ and $P=0.0234$, respectively), but PLP1 (proteolipid protein) is not changed (Fig. 6B). Electron microscopy shows thinner myelin sheaths and occasional degenerating axons with organelle accumulation, dark cytoplasm, or emptied ballooning myelin sheaths in the dorsal corticospinal tract (Fig. 6C and fig. S11G). To specifically measure myelin thickness in this region, we calculated myelin/axon g-ratios and found significant differences ($P<0.001$) across axons of all calibers (Fig. 6D). Although the distribution of myelinated axon size was similar in mutant and wild-type spinal cord, R237H rats demonstrated an increased number of small unmyelinated axons and decreased myelinated axons (Fig. 6D). Measures in optic nerve also show differences in myelin thickness, with no change in size distribution or unmyelinated axon number (Fig. 6E and fig. S12).

GFAP suppression reverses AxD pathology

In comparison with mouse models, the AxD rat demonstrates more robust pathological phenotypes, and clinically relevant motor deficits, which make it an ideal model to test therapeutic compounds. Two of the ASOs designed to target mouse *Gfap* (7) cross react with the rat transcript. A dose-response curve for the most potent ASO shows a reduction in rat *Gfap* transcript with increasing ASO concentrations (Fig. 7A). To determine the effects of incremental decreases in transcript on GFAP protein accumulation and composition, we fractionated lysates from cortex and cervical spinal cord from animals treated with

increasing concentrations of ASO to quantify and compare soluble GFAP (monomers, dimers, and tetramers), polymerized filaments, and RF aggregates (Fig. 7B). The majority of GFAP exists in the filamentous cytoskeletal form (20, 37, 38). As expected, only mutant animals show substantial amounts of GFAP in the RF-enriched fraction. Although both the filamentous and aggregate forms are more resistant to biochemical solubilization, all three pools show a similar decrease with increasing doses of ASO, suggesting that they are in equilibrium. GFAP in CSF and plasma also decreases with increasing dose of ASO (Fig. 7, C and D), again supporting potential utility as a biomarker.

To further test whether ASO treatment can prevent or reverse AxD pathology, we treated two cohorts of R237H rats and wild-type littermates with 300 μg of ASO for maximal suppression (dose response in Fig. 7A): one at 3 weeks of age, immediately after weaning and before onset of obvious clinical phenotypes, and a second group at 8 weeks of age when animals are severely impaired (Fig. 1, F, H and I). Animals in both groups were tested for strength and coordination at 10 weeks after treatment (13 and 18 weeks of age, respectively), and tissues were collected 12 weeks after treatment (15 and 20 weeks of age) to confirm GFAP suppression and assess cellular phenotypes. To confirm GFAP suppression, we quantified both transcript and total protein in hippocampus and spinal cord and found concentrations at or below that of wild-type controls in both treatment groups (Fig. 7, E and F). Additional transcriptional markers associated with astrogliosis including lipocalin2 (*Lcn2*) and the small chemokine *Cxcl10* were normalized by ASO treatment. The marker for microglial activation Iba1 (*Aif1*) was also reduced in R237H treated animals compared with those receiving vehicle (Fig. 7F). Histological assessment confirmed clearance of RFs (Fig. 7G and fig. S13A, hippocampus from rats treated at 8 weeks shown), and immunoblotting demonstrated clearance of high molecular weight ubiquitinated proteins regardless of treatment age (Fig. 7H). Furthermore, treatment of an additional cohort of animals at 3 weeks of age demonstrated sustained GFAP suppression at 24 weeks after treatment (fig. S14).

GFAP suppression rescues motor deficits and AxD phenotypes

We next asked whether the substantial correction in cellular and molecular pathology achieved by ASO administration yielded clinical benefit. After ASO treatment, animals were weighed weekly as a general measure of health and failure to thrive. R237H rats receiving ASO at 3 weeks showed no difference in body weight (Fig. 8A) and were indistinguishable from wild-type littermates (movie S3). R237H rats treated at 8 weeks showed significant improvement [P=0.0001, two-way repeated-measures (RM) analysis of variance (ANOVA)] over time compared with those receiving vehicle (Fig. 8A). ASO treatment in both groups led to increased grip strength and markedly improved performance in the horizontal ladder test (Fig. 8, B and C, animals tested 10 weeks after treatment), with increased speed and reduced slippage (movies S4 to S7; animals treated at 8 weeks shown at 10 weeks after treatment), suggesting that not only could deterioration be prevented but also that functional deficits could be reversed by GFAP clearance. At the cellular level, the appearance of ramified microglia in ASO-treated animals gave further evidence of a quieted neuroinflammatory response (Fig. 8, D to G, and fig. S13B), and in astrocytes, expression of proteins associated with normal astrocyte function such as KCNJ10 and AQP4

was normalized in rats of either age group (Fig. 8, H to O, and fig. S13, C and D, spinal cord of rats treated at 8 weeks; Fig. 8, D to O and fig. S13, tissues collected 12 weeks after treatment).

With the rescue of both cellular and behavioral phenotypes, we wanted to know whether white matter changes in spinal cord could also be prevented or reversed (Fig. 8, P and Q). Area measures of spinal cord cross sections showed that treatment at 3 weeks of age prevented deterioration. Although ASO treatment at 8 weeks of age did not show improvements in spinal cord size, the percentage of white matter increased. In addition, MBP transcript and protein increased in R237H rats treated with ASO at both time points.

DISCUSSION

AxD is a devastating neurological disorder, and GFAP suppression by targeted ASO therapy offers a real possibility for treatment. Our proof-of-concept studies using *Gfap*-targeting ASOs in mouse models demonstrated reversal of AxD pathology, including protein accumulation and aggregation and the reactive stress response (7). However, AxD mice display relatively mild behavioral phenotypes, necessitating animal models with clinically relevant outcome measures in which to test functional improvement. The GFAP-R237H rat has a heavy burden of pathology with high amounts of GFAP, widespread RF formation throughout the brain and spinal cord, myelin deficits and functional deficits including motor impairment, failure to thrive, and increased mortality.

In this study, the severe and progressive phenotype of the R237H rat allowed us to test two treatment strategies to either prevent or reverse behavioral deficits. Treatment of R237H rats with *Gfap*-targeting ASO at weaning cleared molecular and cellular pathology, preventing onset of clinical phenotypes, and R237H rats treated at this age remained physically indistinguishable from wild-type animals. Treatment of severely affected young adult rats not only cleared pathology but also partially reversed white matter deficits and motor impairment, leading to a substantial improvement in overall neurologic function. Recent studies have used ASOs to target neuronal and oligodendrocyte pathology in other degenerative disorders, including Huntington's and Pelizaeus-Merzbacher diseases, respectively (39, 40). Here, we demonstrate that targeting astrocyte-specific *Gfap* rescues astrocyte function in AxD, allowing the recovery of other cell types in the CNS.

AxD is classified as a leukodystrophy, with frontal lobe white matter loss in patients with early onset, and brainstem and cervical cord atrophy nearly universal in those with later onset (2, 41–43). To determine whether R237H rats have myelin deficits, we focused on cervical spinal cord as a relevant and discrete area for histological, molecular, and ultrastructural analysis. Reduced white matter volume, decreased myelin proteins, thin myelin sheaths, and degenerating axons demonstrate clear deficits in R237H rat spinal cord, and thinner sheaths observed in optic nerve suggest these deficits may be more widespread. Although astrocyte dysfunction may directly affect local myelination and spinal cord circuits, deterioration of other brain regions or descending spinal tracts may also contribute to cord atrophy and motor impairment. Future studies to assess CNS connectivity and descending versus ascending tracts in spinal cord, brainstem, and other brain regions

in the rat model could potentially reveal how astrocyte pathology affects long-range relays, local circuits, or central pattern generators in AxD (44–49).

Astrocytes are vital in supporting white matter integrity by maintaining ion and neurotransmitter balance and through the secretion of a variety of myelin-promoting and myelin-inhibiting factors, and other leukodystrophies including megalencephalic leukoencephalopathy with subcortical cysts and vanishing white matter disease are associated with astrocyte dysfunction (50). Altered expression and cellular distribution of SLC1A2, GJA1, AQP4, and KCNJ10, as observed in R237H rat astrocytes, could have profound effects on ion and neurotransmitter homeostasis and myelination. We have also reported that AxD-associated mutations lead to increased brain stiffness (23), and tissue stiffness has been shown to regulate oligodendrocyte progenitor cell (OPC) proliferation and differentiation (51). In addition, recent studies with a human induced pluripotent stem cell (iPSC) model of AxD show a potential connection between elevation of the astrocyte-secreted glycoprotein CHI3L1 (chitinase 3 like 1, YKL-40) and reduced OPC proliferation (52). Although it is still unclear how astrocyte dysfunction leads to white matter deficits in AxD and whether the leukodystrophy reflects hypo- or demyelination, the rat model developed here now offers the opportunity to study these effects in detail.

Whether the changes in expression or polarization of AQP4 can account for the increased water content observed in multiple areas of the brain and spinal cord in R237H rats is not clear. Generally, edema in the context of reduced AQP4 is considered vasogenic in origin (53, 54), yet the blood-brain barrier appeared intact in the R237H rat spinal cord, where the change of water was most notable, at least by the methods used for analysis. In addition, some sites with increased water, such as corpus callosum, showed no evident changes in AQP4 expression. Given that white matter has proportionally less water than gray (55), the decreased white matter volume in spinal cord of R237H rats may also contribute to increased water measured in total cord. Furthermore, both AQP4 and the movement of interstitial fluid through the parenchyma via the glymphatic system can be altered in the setting of chronic astrogliosis (56). Determining how astrocyte dysfunction in AxD affects glymphatic flux and clearance of metabolic waste in the CNS will be an important focus of future study.

Early onset AxD is often associated with failure to thrive (2), and decreased body weight is a consistent feature among AxD rodent models (9, 57). R237H rats achieve normal early postnatal milestones, but they fail to gain weight after weaning and never reach the size of their wild-type littermates. Oropharyngeal dysphagia and frequent emesis are also common features in AxD that may contribute to body weight differences (2, 58) and remain to be investigated in the model. Although rodents cannot vomit (59), surrogate measures of nausea such as pica behavior (60) and treatment with antiemetics may inform whether brainstem pathology affects the chemoreceptor trigger zone in R237H rats. Intractable vomiting is also observed in neuromyelitis optica (NMO) spectrum disorders, where the autoimmune response against the high concentration of APQ4 in circumventricular organs can lead to area postrema syndrome (61), suggesting that astrocyte dysfunction may be a common denominator for frequent emesis in both AxD and NMO. Several studies have also tied astrocyte function to hypothalamic regulation of food intake and energy balance (62–65),

and a detailed analysis of brainstem and hypothalamus will be essential in determining causes for failure to thrive and lethality in the model.

Several limitations of our study are discussed above, but others are also worth noting. Although the rat model replicates key clinical phenotypes of AxD, particularly motor impairment, we have not evaluated whether the animals have seizures, which are often prominent in early-onset AxD and could also contribute to the increased mortality observed in the rat. In addition, R237H rats demonstrate substantial cortical and hippocampal pathology including deficits in adult neurogenesis, and studies are underway to assess cognitive behavior. Another critical consideration for GFAP suppression as a therapeutic strategy is the increased astrocyte complexity in humans and the potential for unanticipated consequences. GFAP knockout mice are more vulnerable to CNS injury but exhibit no overt phenotypes (66), and here, we show that GFAP-null rats are also ostensibly normal. Although we can achieve nearly complete knockdown of GFAP in the models, the same suppression may not be possible or desirable in human, and future efforts will focus on determining the amount of reduction necessary to relieve relevant phenotypes in the R237H rat.

Gfap-targeting ASO treatment leads to long-lasting suppression of GFAP transcript and protein in both mouse and rat models of AxD. We have found that ASO treatment can not only prevent but also reverse many aspects of disease in the rat model developed for this study and that functional improvement is possible even when treatment is delayed until the animals are already severely impaired. Although the ASOs used in this study were selected to target rodent *Gfap*, efforts to test human *GFAP*-targeted ASO in clinical trials are underway.

MATERIALS AND METHODS

Study design

Our goal for this study was to develop a preclinical model of AxD with relevant pathological and behavioral phenotypes to facilitate studies of pathophysiology and testing of potential therapeutics. The targeted mutation in the rat GFAP gene was chosen on the basis of the severity and frequency of the R239H mutation in human disease. Rats were used for their increased potential for functional phenotypes compared with the mouse and the wealth of literature on behavioral research. Generation of the R237H rat was contracted through Applied StemCell, Inc., and first-generation offspring were bred and analyzed at the University of Wisconsin – Madison. All animal studies were approved by the College of Letters and Sciences and Vice Chancellor's Office for Research and Graduate Education Animal Care and Use Committee.

Experimental approach was based on the following goals: (i) to confirm the targeted mutation and to breed transgenic animals to wild-type rats to remove potential off-target mutations; (ii) to confirm the presence of hallmark AxD pathology including Rosenthal fibers and the astrocyte stress response; (iii) to identify cell- and non-cell-autonomous effects of GFAP mutation; (iv) to identify behavioral phenotypes relevant to AxD; and (v) to

test *Gfap*-targeted ASOs to validate the model and as a promising therapeutic to prevent or rescue behavioral phenotypes.

Animal numbers for each experiment were determined by our previous experience with mouse models of AxD. Both sexes were used for experiments, and in some cases, females were used preferentially because of their smaller size for long-term cohousing. ASO treatment ages and endpoints were determined prospectively on the basis of the progression of the rat phenotype and time course studies in the mouse. A small number of R237H rats were removed from studies because of death or euthanasia of moribund animals. Rats were randomly assigned sequential numerical identifiers before weaning and genotyping, and treatment assignments were alternated within sex and genotype groups in the order of the identification number. No more than two animals per group (sex, genotype, and treatment) were taken from a single litter. Outliers were only excluded if the result reflected technical failure (such as low normalization signal indicating sample loss).

Laboratory staff performing behavioral assays or measurements were blinded to genotype and treatment, and those performing molecular and histological analyses were blinded until after data collection when possible. Given the severity of the pathology and physical phenotype of the R237H rat, blinding was not always possible.

Statistical analysis

Technical replicates were included for all molecular analyses (quantitative polymerase chain reaction and enzyme-linked immunosorbent assay), and averaged per animal. All data points are shown with the mean and SD error bars, unless noted otherwise. Statistics are based on animal numbers per group and do not include technical replicates. Typically, two-tailed unpaired *t* tests were used for comparisons of two groups, one-way ANOVA with Tukey's (all groups compared) or Dunnett's (groups compared to control) multiple comparisons for comparisons of multiple groups under the same conditions, multiple *t* tests for comparisons of different measures between two groups, two-way ANOVA with Tukey's multiple comparisons for tests with two conditions, and two-way RM ANOVA with Sidak's multiple comparisons to compare two groups over time. Tests used are indicated in the figure legends. GraphPad Prism v6 was used for statistical analysis and graphing.

Supplementary Material

Refer to Web version on PubMed Central for supplementary material.

Acknowledgments

We would like to thank Denice Springman, Rebecca Pulvermacher, Jacob Loeffelholz, and Alder Levin for technical support.

Funding:

This work was supported by grants from the NIH NICHD (HD076892 to A.M., HD03352 and HD090256 core grants to the Waisman Center, and HD103526 to the Univ. California MIND Institute IDDRCs), NINDS (NS110719 to T.L.H.), CLIMB (Children Living with Inherited Metabolic Disease, Cheshire, UK), and by the Juanma Fund. M.-D.P. was funded by The Ministry of Science and Technology (108–2918-I-007–013) and the Waisman Scholar fund.

Data and materials availability:

All data associated with this study are present in the paper or the Supplementary Materials. The mutant rats will be available through the Rat Resource and Research Center at the University of Missouri in Columbia, MO (Gfap-null, RRRC#931; Gfap-R237H KI, RRRC#932).

REFERENCES AND NOTES

1. Brenner M, Johnson AB, Boespflug-Tanguy O, Rodriguez D, Goldman JE, Messing A, Mutations in GFAP, encoding glial fibrillary acidic protein, are associated with Alexander disease. Nat Genet 27, 117–120 (2001). [PubMed: 11138011]
2. Prust M, Wang J, Morizono H, Messing A, Brenner M, Gordon E, Hartka T, Sokohl A, Schiffmann R, Gordish-Dressman H, Albin R, Amartino H, Brockman K, Dinopoulos A, Dotti MT, Fain D, Fernandez R, Ferreira J, Fleming J, Gill D, Griebel M, Heilstedt H, Kaplan P, Lewis D, Nakagawa M, Pedersen R, Reddy A, Sawaishi Y, Schneider M, Sherr E, Takiyama Y, Wakabayashi K, Gorospe JR, Vanderver A, GFAP mutations, age at onset, and clinical subtypes in Alexander disease. Neurology 77, 1287–1294 (2011). [PubMed: 21917775]
3. Messing A, Brenner M, Feany MB, Nedergaard M, Goldman JE, Alexander disease. J Neurosci 32, 5017–5023 (2012). [PubMed: 22496548]
4. Olabarria M, Goldman JE, Disorders of Astrocytes: Alexander Disease as a Model. Annu Rev Pathol 12, 131–152 (2017). [PubMed: 28135564]
5. Brenner M, Goldman JE, Quinlan RA, Messing A, in Astrocytes in Pathophysiology of the Nervous System, Parpura V, Haydon PG, Eds. (Springer, 2009), chap. 24, pp. 591–648.
6. Bennett CF, Krainer AR, Cleveland DW, Antisense Oligonucleotide Therapies for Neurodegenerative Diseases. Annu Rev Neurosci 42, 385–406 (2019). [PubMed: 31283897]
7. Hagemann TL, Powers B, Mazur C, Kim A, Wheeler S, Hung G, Swayze E, Messing A, Antisense suppression of glial fibrillary acidic protein as a treatment for Alexander disease. Ann Neurol 83, 27–39 (2018). [PubMed: 29226998]
8. Hagemann TL, Paylor R, Messing A, Deficits in adult neurogenesis, contextual fear conditioning, and spatial learning in a Gfap mutant mouse model of Alexander disease. J Neurosci 33, 18698–18706 (2013). [PubMed: 24259590]
9. Hagemann TL, Connor JX, Messing A, Alexander disease-associated glial fibrillary acidic protein mutations in mice induce Rosenthal fiber formation and a white matter stress response. J Neurosci 26, 11162–11173 (2006). [PubMed: 17065456]
10. Hagemann TL, Gaeta SA, Smith MA, Johnson DA, Johnson JA, Messing A, Gene expression analysis in mice with elevated glial fibrillary acidic protein and Rosenthal fibers reveals a stress response followed by glial activation and neuronal dysfunction. Hum Mol Genet 14, 2443–2458 (2005). [PubMed: 16014634]
11. Gomi H, Yokoyama T, Fujimoto K, Ikeda T, Katoh A, Itoh T, Itohara S, Mice devoid of the glial fibrillary acidic protein develop normally and are susceptible to scrapie prions. Neuron 14, 29–41 (1995). [PubMed: 7826639]
12. Pekny M, Leveen P, Pekna M, Eliasson C, Berthold CH, Westermark B, Betsholtz C, Mice lacking glial fibrillary acidic protein display astrocytes devoid of intermediate filaments but develop and reproduce normally. EMBO J. 14, 1590–1598 (1995). [PubMed: 7737111]
13. Liedtke W, Edelmann W, Bieri PL, Chiu FC, Cowan NJ, Kucherlapati R, Raine CS, GFAP is necessary for the integrity of CNS white matter architecture and long-term maintenance of myelination. Neuron 17, 607–615 (1996). [PubMed: 8893019]
14. McCall MA, Gregg RG, Behringer RR, Brenner M, Delaney CL, Galbreath EJ, Zhang CL, Pearce RA, Chiu SY, Messing A, Targeted deletion in astrocyte intermediate filament (Gfap) alters neuronal physiology. Proc Natl Acad Sci U S A 93, 6361–6366 (1996). [PubMed: 8692820]

15. Chen MH, Hagemann TL, Quinlan RA, Messing A, Perng MD, Caspase cleavage of GFAP produces an assembly-compromised proteolytic fragment that promotes filament aggregation. ASN Neuro 5, e00125 (2013). [PubMed: 24102621]
16. Battaglia RA, Beltran AS, Delic S, Dumitru R, Robinson JA, Kabiraj P, Herring LE, Madden VJ, Ravinder N, Willems E, Newman RA, Quinlan RA, Goldman JE, Perng MD, Inagaki M, Snider NT, Site-specific phosphorylation and caspase cleavage of GFAP are new markers of Alexander disease severity. Elife 8, e47789 (2019). [PubMed: 31682229]
17. Tomokane N, Iwaki T, Tateishi J, Iwaki A, Goldman JE, Rosenthal fibers share epitopes with alpha B-crystallin, glial fibrillary acidic protein, and ubiquitin, but not with vimentin. Immunoelectron microscopy with colloidal gold. Am J Pathol 138, 875–885 (1991). [PubMed: 1707236]
18. Lach B, Sikorska M, Rippstein P, Gregor A, Staines W, Davie TR, Immunoelectron microscopy of Rosenthal fibers. Acta Neuropathol 81, 503–509 (1991). [PubMed: 1650112]
19. Zatloukal K, Stumptner C, Fuchsbichler A, Heid H, Schnoelzer M, Kenner L, Kleinert R, Prinz M, Aguzzi A, Denk H, p62 Is a common component of cytoplasmic inclusions in protein aggregation diseases. Am J Pathol 160, 255–263 (2002). [PubMed: 11786419]
20. Heaven MR, Flint D, Randall SM, Sosunov AA, Wilson L, Barnes S, Goldman JE, Muddiman DC, Brenner M, Composition of Rosenthal fibers, the protein aggregate hallmark of Alexander disease. J Proteome Res 15, 2265–2282 (2016). [PubMed: 27193225]
21. Jany PL, Hagemann TL, Messing A, GFAP expression as an indicator of disease severity in mouse models of Alexander disease. ASN Neuro 5, art:e00109.doi:00110.01042/AN20130003 (2013).
22. Moody LR, Barrett-Wilt GA, Sussman MR, Messing A, Glial fibrillary acidic protein exhibits altered turnover kinetics in a mouse model of Alexander disease. J Biol Chem 292, 5814–5824 (2017). [PubMed: 28223355]
23. Wang L, Xia J, Li J, Hagemann TL, Jones JR, Fraenkel E, Weitz DA, Zhang SC, Messing A, Feany MB, Tissue and cellular rigidity and mechanosensitive signaling activation in Alexander disease. Nat Commun 9, 1899 (2018). [PubMed: 29765022]
24. Sofroniew MV, Astrogliosis. Cold Spring Harb Perspect Biol 7, a020420 (2014). [PubMed: 25380660]
25. Cho W, Messing A, Properties of astrocytes cultured from GFAP over-expressing and GFAP mutant mice. Exp Cell Res 315, 1260–1272 (2009). [PubMed: 19146851]
26. Chen YS, Lim SC, Chen MH, Quinlan RA, Perng MD, Alexander disease causing mutations in the C-terminal domain of GFAP are deleterious both to assembly and network formation with the potential to both activate caspase 3 and decrease cell viability. Exp Cell Res 317, 2252–2266 (2011). [PubMed: 21756903]
27. Acarin L, Villapol S, Faiz M, Rohn TT, Castellano B, Gonzalez B, Caspase-3 activation in astrocytes following postnatal excitotoxic damage correlates with cytoskeletal remodeling but not with cell death or proliferation. Glia 55, 954–965 (2007). [PubMed: 17487878]
28. Aras R, Barron AM, Pike CJ, Caspase activation contributes to astrogliosis. Brain Res 1450, 102–115 (2012). [PubMed: 22436850]
29. Guyenet SJ, Nguyen HT, Hwang BH, Schwartz MW, Baskin DG, Thaler JP, High-fat diet feeding causes rapid, non-apoptotic cleavage of caspase-3 in astrocytes. Brain Res 1512, 97–105 (2013). [PubMed: 23548599]
30. Stevenson ME, Lensmire NA, Swain RA, Astrocytes and radial glia-like cells, but not neurons, display a nonapoptotic increase in caspase-3 expression following exercise. Brain Behav 8, e01110 (2018). [PubMed: 30240148]
31. Villapol S, Acarin L, Faiz M, Castellano B, Gonzalez B, Survivin and heat shock protein 25/27 colocalize with cleaved caspase-3 in surviving reactive astrocytes following excitotoxicity to the immature brain. Neuroscience 153, 108–119 (2008). [PubMed: 18358624]
32. Tian R, Wu X, Hagemann TL, Sosunov AA, Messing A, McKhann GM, Goldman JE, Alexander disease mutant glial fibrillary acidic protein compromises glutamate transport in astrocytes. J Neuropathol Exp Neurol 69, 335–345 (2010). [PubMed: 20448479]
33. Nagelhus EA, Mathiisen TM, Ottersen OP, Aquaporin-4 in the central nervous system: cellular and subcellular distribution and coexpression with KIR4.1. Neuroscience 129, 905–913 (2004). [PubMed: 15561407]

34. Cammer W, Zhang H, Atypical localization of the oligodendrocytic isoform (PI) of glutathione-S-transferase in astrocytes during cuprizone intoxication. J Neurosci Res 36, 183–190 (1993). [PubMed: 8263971]
35. Lee HN, Jeon GS, Kim DW, Cho IH, Cho SS, Expression of adenomatous polyposis coli protein in reactive astrocytes in hippocampus of kainic acid-induced rat. Neurochem Res 35, 114–121 (2010). [PubMed: 19655246]
36. Leroy K, Duyckaerts C, Bovekamp L, Müller O, Anderton BH, Brion JP, Increase of adenomatous polyposis coli immunoreactivity is a marker of reactive astrocytes in Alzheimer's disease and in other pathological conditions. Acta Neuropathol 102, 1–10 (2001). [PubMed: 11547943]
37. Hsiao VC, Tian R, Long H, Der Perng M, Brenner M, Quinlan RA, Goldman JE, Alexander-disease mutation of GFAP causes filament disorganization and decreased solubility of GFAP. J Cell Sci 118, 2057–2065 (2005). [PubMed: 15840648]
38. Robert A, Hookway C, Gelfand VI, Intermediate filament dynamics: What we can see now and why it matters. Bioessays 38, 232–243 (2016). [PubMed: 26763143]
39. Smith AV, Tabrizi SJ, Therapeutic Antisense Targeting of Huntingtin. DNA Cell Biol 39, 154–158 (2020). [PubMed: 31821021]
40. Elitt MS, Barbar L, Shick HE, Powers BE, Maeno-Hikichi Y, Madhavan M, Allan KC, Nawash BS, Gevorgyan AS, Hung S, Nevin ZS, Olsen HE, Hitomi M, Schlatzer DM, Zhao HT, Swayze A, LePage DF, Jiang W, Conlon RA, Rigo F, Tesar PJ, Suppression of proteolipid protein rescues Pelizaeus-Merzbacher disease. Nature 585, 397–403 (2020). [PubMed: 32610343]
41. Russo LS Jr., Aron A, Anderson PJ, Alexander's disease: a report and reappraisal. Neurology 26, 607–614 (1976). [PubMed: 180453]
42. van der Knaap MS, Ramesh V, Schiffmann R, Blaser S, Kyllerman M, Gholkar A, Ellison DW, van der Voorn JP, van Dooren SJ, Jakobs C, Barkhof F, Salomons GS, Alexander disease: ventricular garlands and abnormalities of the medulla and spinal cord. Neurology 66, 494–498 (2006). [PubMed: 16505300]
43. Graff-Radford J, Schwartz K, Gavrilova RH, Lachance DH, Kumar N, Neuroimaging and clinical features in type II (late-onset) Alexander disease. Neurology 82, 49–56 (2014). [PubMed: 24306001]
44. Ozdinler PH, Benn S, Yamamoto TH, Guzel M, Brown RH Jr., Macklis JD, Corticospinal motor neurons and related subcerebral projection neurons undergo early and specific neurodegeneration in hSOD1^{G93A} transgenic ALS mice. J Neurosci 31, 4166–4177 (2011). [PubMed: 21411657]
45. Molofsky AV, Kelley KW, Tsai HH, Redmond SA, Chang SM, Madireddy L, Chan JR, Baranzini SE, Ullian EM, Rowitch DH, Astrocyte-encoded positional cues maintain sensorimotor circuit integrity. Nature 509, 189–194 (2014). [PubMed: 24776795]
46. Kelley KW, Ben Haim L, Schirmer L, Tyzack GE, Tolman M, Miller JG, Tsai HH, Chang SM, Molofsky AV, Yang Y, Patani R, Lakatos A, Ullian EM, Rowitch DH, Kir4.1-Dependent Astrocyte-Fast Motor Neuron Interactions Are Required for Peak Strength. Neuron 98, 306–319.e307 (2018). [PubMed: 29606582]
47. Blumenstock S, Dudanova I, Cortical and Striatal Circuits in Huntington's Disease. Front Neurosci 14, 82 (2020). [PubMed: 32116525]
48. Broadhead MJ, Miles GB, Bi-Directional Communication Between Neurons and Astrocytes Modulates Spinal Motor Circuits. Front Cell Neurosci 14, 30 (2020). [PubMed: 32180706]
49. Khakh BS, Sofroniew MV, Diversity of astrocyte functions and phenotypes in neural circuits. Nat Neurosci 18, 942–952 (2015). [PubMed: 26108722]
50. Lundgaard I, Osório MJ, Kress BT, Sanggaard S, Nedergaard M, White matter astrocytes in health and disease. Neuroscience 276, 161–173 (2014). [PubMed: 24231735]
51. Segel M, Neumann B, Hill MFE, Weber IP, Viscomi C, Zhao C, Young A, Agley CC, Thompson AJ, Gonzalez GA, Sharma A, Holmqvist S, Rowitch DH, Franze K, Franklin RJM, Chalut KJ, Niche stiffness underlies the ageing of central nervous system progenitor cells. Nature 573, 130–134 (2019). [PubMed: 31413369]
52. Li L, Tian E, Chen X, Chao J, Klein J, Qu Q, Sun G, Sun G, Huang Y, Warden CD, Ye P, Feng L, Li X, Cui Q, Sultan A, Douvaras P, Fossati V, Sanjana NE, Riggs AD, Shi Y, GFAP Mutations

in Astrocytes Impair Oligodendrocyte Progenitor Proliferation and Myelination in an hiPSC Model of Alexander Disease. Cell Stem Cell 23, 239–251.e236 (2018). [PubMed: 30075130]

53. Verkman AS, Binder DK, Bloch O, Auguste K, Papadopoulos MC, Three distinct roles of aquaporin-4 in brain function revealed by knockout mice. Biochim Biophys Acta 1758, 1085–1093 (2006). [PubMed: 16564496]
54. Papadopoulos MC, Manley GT, Krishna S, Verkman AS, Aquaporin-4 facilitates reabsorption of excess fluid in vasogenic brain edema. Faseb j 18, 1291–1293 (2004). [PubMed: 15208268]
55. Schwab M, Bauer R, Zwiener U, The distribution of normal brain water content in Wistar rats and its increase due to ischemia. Brain Res 749, 82–87 (1997). [PubMed: 9070630]
56. Mestre H, Kostrikov S, Mehta RI, Nedergaard M, Perivascular spaces, glymphatic dysfunction, and small vessel disease. Clin Sci (Lond) 131, 2257–2274 (2017). [PubMed: 28798076]
57. Messing A, Head MW, Galles K, Galbreath EJ, Goldman JE, Brenner M, Fatal encephalopathy with astrocyte inclusions in GFAP transgenic mice. Am J Pathol 152, 391–398 (1998). [PubMed: 9466565]
58. van der Knaap MS, Naidu S, Breiter SN, Blaser S, Stroink H, Springer S, Begeer JC, van Coster R, Barth PG, Thomas NH, Valk J, Powers JM, Alexander disease: diagnosis with MR imaging. AJNR Am J Neuroradiol 22, 541–552 (2001). [PubMed: 11237983]
59. Horn CC, Kimball BA, Wang H, Kaus J, Dienel S, Nagy A, Gathright GR, Yates BJ, Andrews PL, Why can't rodents vomit? A comparative behavioral, anatomical, and physiological study. PLoS One 8, e60537 (2013). [PubMed: 23593236]
60. Takeda N, Hasegawa S, Morita M, Matsunaga T, Pica in rats is analogous to emesis: an animal model in emesis research. Pharmacol Biochem Behav 45, 817–821 (1993). [PubMed: 8415820]
61. Pittock SJ, Lucchinetti CF, Neuromyelitis optica and the evolving spectrum of autoimmune aquaporin-4 channelopathies: a decade later. Ann N Y Acad Sci 1366, 20–39 (2016). [PubMed: 26096370]
62. Kim JG, Suyama S, Koch M, Jin S, Argente-Arizon P, Argente J, Liu ZW, Zimmer MR, Jeong JK, Szigeti-Buck K, Gao Y, Garcia-Caceres C, Yi CX, Salmaso N, Vaccarino FM, Chowen J, Diano S, Dietrich MO, Tschop MH, Horvath TL, Leptin signaling in astrocytes regulates hypothalamic neuronal circuits and feeding. Nat Neurosci 17, 908–910 (2014). [PubMed: 24880214]
63. Fuente-Martín E, García-Cáceres C, Argente-Arizón P, Díaz F, Granado M, Freire-Regatillo A, Castro-González D, Ceballos ML, Frago LM, Dickson SL, Argente J, Chowen JA, Ghrelin Regulates Glucose and Glutamate Transporters in Hypothalamic Astrocytes. Sci Rep 6, 23673 (2016). [PubMed: 27026049]
64. Fuente-Martín E, García-Cáceres C, Granado M, de Ceballos ML, Sánchez-Garrido M, Sarman B, Liu ZW, Dietrich MO, Tena-Sempere M, Argente-Arizón P, Díaz F, Argente J, Horvath TL, Chowen JA, Leptin regulates glutamate and glucose transporters in hypothalamic astrocytes. J Clin Invest 122, 3900–3913 (2012). [PubMed: 23064363]
65. Chowen JA, Frago LM, Fernández-Alfonso MS, Physiological and pathophysiological roles of hypothalamic astrocytes in metabolism. J Neuroendocrinol 31, e12671 (2019). [PubMed: 30561077]
66. Messing A, Brenner M, GFAP at 50. ASN Neuro 12, 1759091420949680 (2020). [PubMed: 32811163]
67. Neely JD, Christensen BM, Nielsen S, Agre P, Heterotetrameric composition of aquaporin-4 water channels. Biochemistry 38, 11156–11163 (1999). [PubMed: 10460172]
68. Bjerrum OJ, Schafer-Nielsen C, Buffer systems and transfer parameters for semidry electroblotting with a horizontal apparatus Analytical Electrophoresis (Verlag Chemie, Weinheim, Germany, 1986).
69. Bolte S, Cordelières FP, A guided tour into subcellular colocalization analysis in light microscopy. J Microsc 224, 213–232 (2006). [PubMed: 17210054]
70. Smith TG Jr., Lange GD, Marks WB, Fractal methods and results in cellular morphology--dimensions, lacunarity and multifractals. J Neurosci Methods 69, 123–136 (1996). [PubMed: 8946315]

71. Lundgaard I, Wang W, Eberhardt A, Vinitsky HS, Reeves BC, Peng S, Lou N, Hussain R, Nedergaard M, Beneficial effects of low alcohol exposure, but adverse effects of high alcohol intake on glymphatic function. Sci Rep 8, 2246 (2018). [PubMed: 29396480]

72. Metz GA, Whishaw IQ, The ladder rung walking task: a scoring system and its practical application. J Vis Exp, e1204 (2009).

73. Metz GA, Whishaw IQ, Cortical and subcortical lesions impair skilled walking in the ladder rung walking test: a new task to evaluate fore- and hindlimb stepping, placing, and co-ordination. J Neurosci Methods 115, 169–179 (2002). [PubMed: 11992668]

74. Frankowski JC, DeMars KM, Ahmad AS, Hawkins KE, Yang C, Leclerc JL, Dore S, Candelario-Jalil E, Detrimental role of the EP1 prostanoid receptor in blood-brain barrier damage following experimental ischemic stroke. Sci Rep 5, 17956 (2015). [PubMed: 26648273]

75. Liddelow SA, Guttenplan KA, Clarke LE, Bennett FC, Bohlen CJ, Schirmer L, Bennett ML, Munch AE, Chung WS, Peterson TC, Wilton DK, Frouin A, Napier BA, Panicker N, Kumar M, Buckwalter MS, Rowitch DH, Dawson VL, Dawson TM, Stevens B, Barres BA, Neurotoxic reactive astrocytes are induced by activated microglia. Nature 541, 481–487 (2017). [PubMed: 28099414]

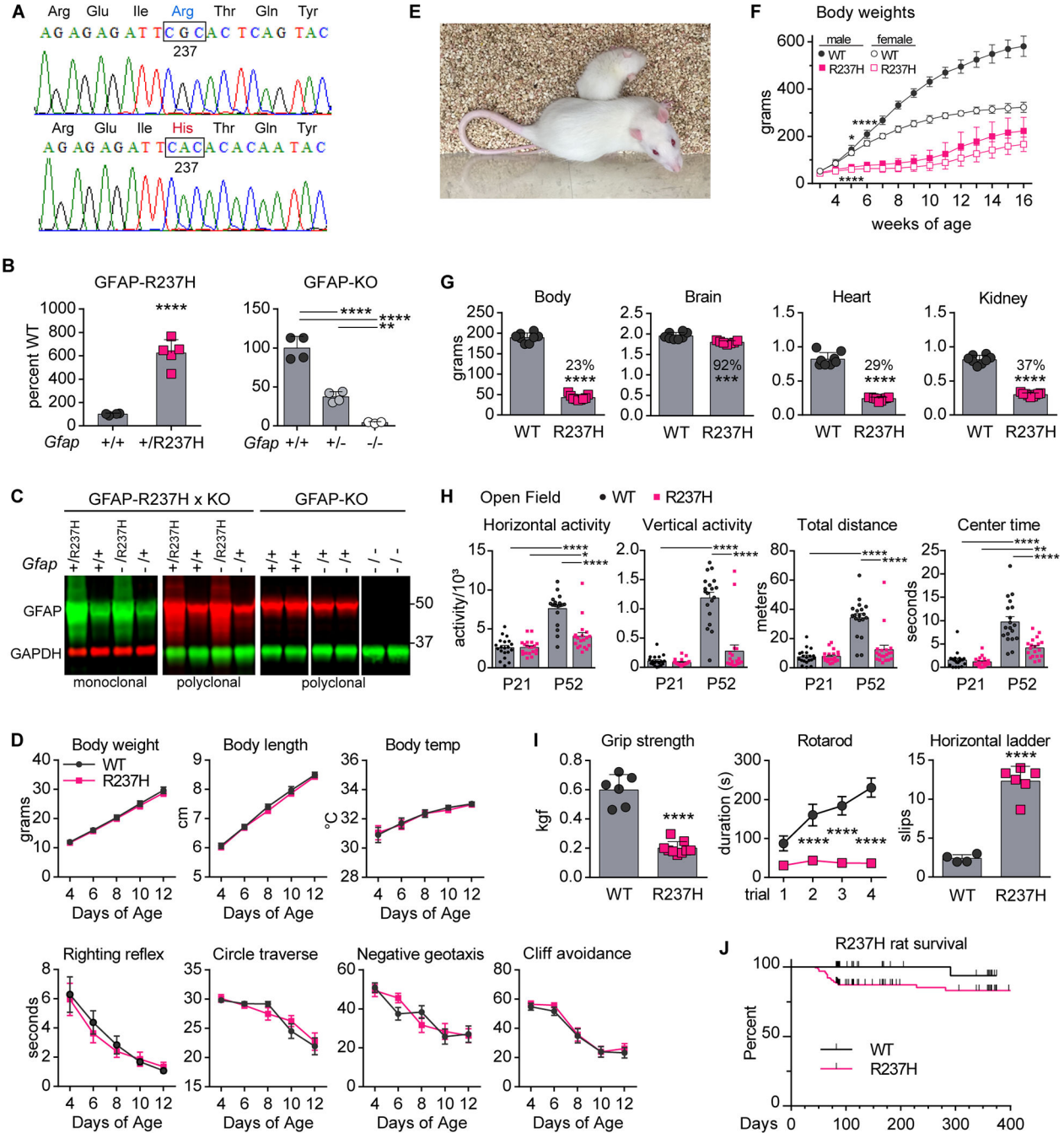

Fig. 1. Validation and phenotyping of GFAP mutant rat model.

(**A**) Sequence analysis of complementary DNA from R237H rat brain showing CRISPR-Cas9 targeting for AxD-associated missense mutation. (**B**) Quantification of *Gfap* transcript in R237H rat brain compared with wild type (WT) at postnatal day 21 (P21; left panel, **** $P < 0.0001$, two-tailed t test, n = 4 WT and n = 5 R237H) and in a second line harboring a *Gfap* frameshift mutation (heterozygous and homozygous, P30, right panel; **** $P < 0.0001$ and ** $P = 0.0069$, one-way ANOVA, Tukey's multiple comparisons, n = 4 +/+, 4 +/−, and 3 −/−). (**C**) Western analysis of total protein from GFAP point mutant

(R237H) and knockout (KO) rat brains with both monoclonal (GA5) and polyclonal (DAKO Z0334) antibodies. Crosses between the two lines to combine mutant and null alleles (*Gfap* –/R237H) show expression of the R237H targeted allele in the left panels (GFAP-R237H × KO offspring at 8 weeks). Analysis of GFAP-KO rats at P30 is shown in the right panel and molecular weight markers are indicated on the right: 50 and 37 kD. (**D**) Developmental milestone assessment of R237H rats during the first two postnatal weeks, $P > 0.5$ for effect of genotype, two-way repeated-measures ANOVA, n = 15 litters consisting of 39 WT (20 male, 19 female) and 39 R237H (19 male, 20 female), error = SEM. (**E**) Image of R237H (top) and WT (bottom) male littermates at 8 weeks of age. (**F**) Body weight comparisons of R237H and WT rats after weaning at 3 weeks of age (two-way repeated measures ANOVA, Sidak's multiple comparisons show significant differences by 5 weeks of age, $*P = 0.0138$, males, $****P < 0.0001$, females; weeks 6 to 13, $****P < 0.0001$ for males and females, n = 5 WT males, n = 6 WT females, n = 4 R237H males, n = 4 R237H females). (**G**) Organ weights of R237H rats compared with WT. Percent of WT shown for R237H, $***P = 0.0006$ and $****P < 0.0001$, two-tailed *t* test, females at 10 weeks, n = 8 WT and n = 9 R237H. (**H**) Open field measures of R237H and WT rat activity at P21 and P52 [two-way ANOVA, Tukey's multiple comparisons, n = 10 (5 males, 5 females) per genotype, error = SEM]. (**I**) Measures of forelimb grip strength ($****P < 0.0001$, two-tailed *t* test, females at 8 weeks, n = 6 WT and n = 9 R237H), rotarod performance (two-way repeated measures ANOVA, with Sidak's multiple comparisons, $****P < 0.0001$, males and females at 8 weeks, n = 9 WT and n = 11 R237H, error = SEM), and average number of slips per run on a horizontal ladder ($****P < 0.0001$, two-tailed *t* test, females at 8 weeks, n = 4 WT and n = 6 R237H) in R237H rats compared with WT littermates. kgf, kilogram force. (**J**) Kaplan-Meyer curve of survival rates of R237H rats aged to 12 weeks or more ($P = 0.0008$, Mantel-Cox test, n = 165 R237H and n = 98 WT male and female rats). Black tick marks indicate animals removed for experiments.

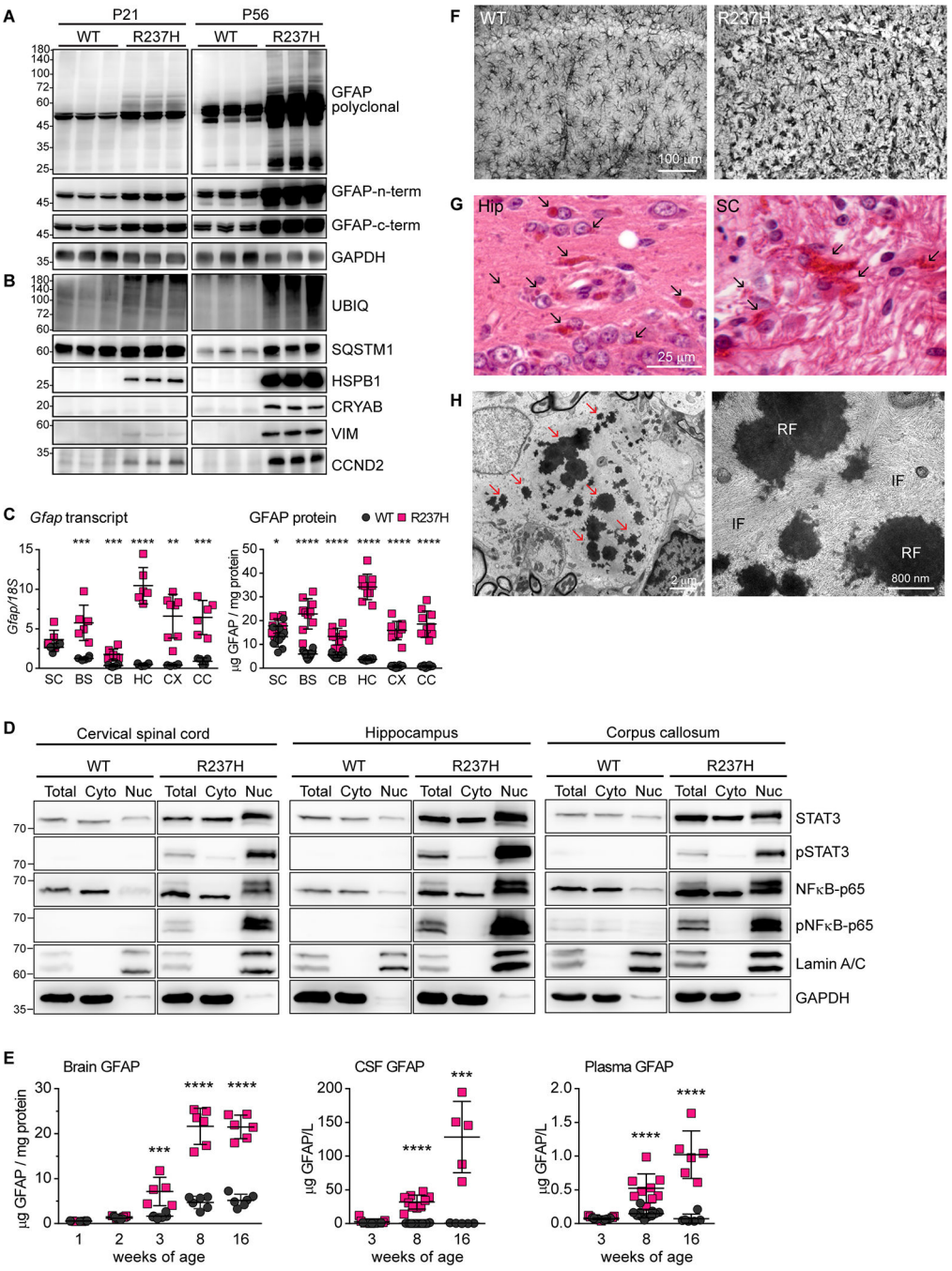

Fig. 2. GFAP accumulation, RFs, and astrogliosis in R237H rats.

(**A**) Western analysis of GFAP protein at P21 and P56 in R237H and WT rat brain. Three different antibodies including a polyclonal and two monoclonal antibodies targeting the N and C termini are used to verify the presence and size of GFAP from mutant animals (molecular weight marker sizes are indicated at left). (**B**) Western analysis of proteins associated with RFs and astrocyte pathology in AxD. Lanes represent individual animals. (**C**) Regional transcript [quantitative polymerase chain reaction (qPCR)] and protein [enzyme-linked immunosorbent assay (ELISA)] analysis at 8 weeks of age (both

sexes, *$P < 0.05$, **$P < 0.01$, ***$P < 0.001$, and ****$P < 0.0001$, multiple *t* tests, Holm-Sidak correction method, $\alpha = 5\%$, n = 4 to 6 WT and n = 5 to 7 R237H for transcript, and n = 10 for protein). (**D**) Western analysis of total protein and subcellular biochemical fractions from cervical spinal cord, hippocampus, and corpus callosum for phosphorylated STAT3 and NFκB in cytosolic (Cyto) and nuclear (Nuc) compartments of R237H rat CNS. Lamin A/C is used as a nuclear protein control (N = 4, representative blots shown). (**E**) GFAP-ELISA of brain homogenates, CSF, and plasma from R237H rats at different ages (***$P < 0.001$ and **** $P < 0.0001$, multiple *t* tests, Holm-Sidak correction method, $\alpha = 5\%$, n = 6 WT, n = 5 to 6 R237H for brain, n = 7, 14, and 5 WT and 8, 10, and 5 R237H at 3, 8, and 16 weeks, respectively, for CSF, n = 8, 11, and 6 WT and n = 7, 9, and 6 R237H at 3, 8, and 16 weeks, respectively, for plasma). (**F**) GFAP immunohistochemistry in hippocampus (CA1) at 8 weeks of age. (**G**) Hematoxylin and eosin (H&E) stain shows RFs as eosinophilic inclusions and puncta (arrows, not all indicated) in hippocampus (Hip) and spinal cord (SC) at 8 weeks of age. (**H**) Electron microscopy shows hallmark RFs as dense osmiophilic aggregates ensnared in a bed of intermediate filaments (arrows on left panel indicate representative fibers; enlarged in right panel). IF, intermediate filaments.

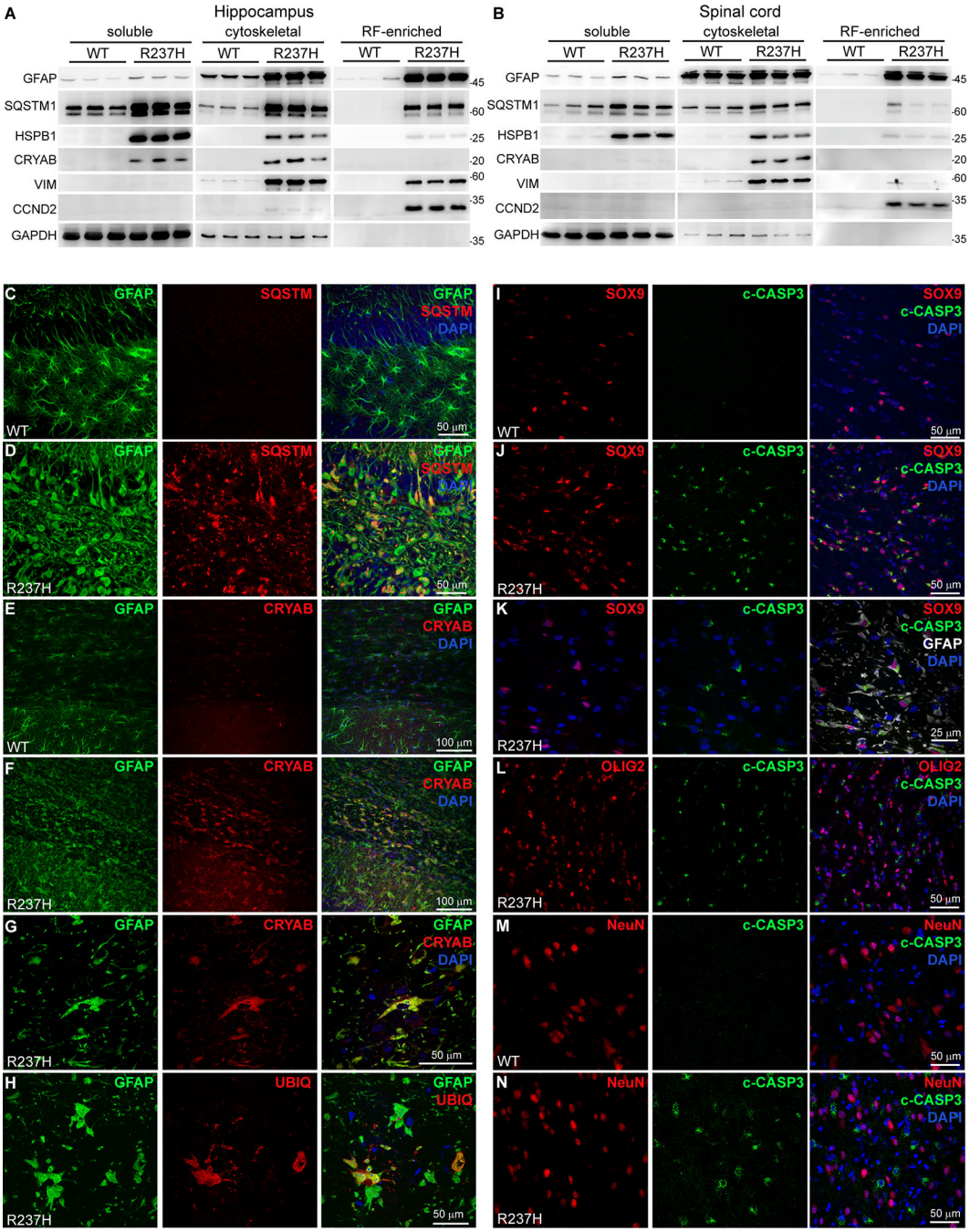

Fig. 3. Astrocyte stress response and pathology in R237H rats.

(**A** and **B**) Western analysis of soluble, cytoskeletal, and RF-enriched fractions for GFAP and other RF-associated proteins in hippocampus (**A**) and cervical spinal cord (**B**), n = 3, with each lane representing individual animals at 8 weeks of age. (**C** and **D**) Immunofluorescence labeling (IF) of SQSTM1 and GFAP in R237H and WT rat hippocampus (dentate gyrus). (**E** to **G**) CRYAB- and GFAP-IF in R237H corpus callosum (**F** and **G**) in contrast to WT animals (**E**). (**H**) UBIQ- and GFAP-IF in R237H astrocytes in the hippocampal stratum lacunosum moleculare. (**I** to **K**) Cleaved caspase-3-positive

astrocytes colabeled with Sox9- and GFAP-IF in corpus callosum from R237H rats. (**L** to **N**) Colabeling of cleaved caspase-3 with markers for other cell types including those of the oligodendrocyte lineage (**L**; OLIG2, corpus callosum) and neurons (**M** and **N**; NeuN, brainstem) in R237H rats. Confocal images are single optical slices, and camera and microscope settings were equivalent for comparisons between genotypes (n = 4 to 5 animals per genotype, males and females at 8 weeks of age).

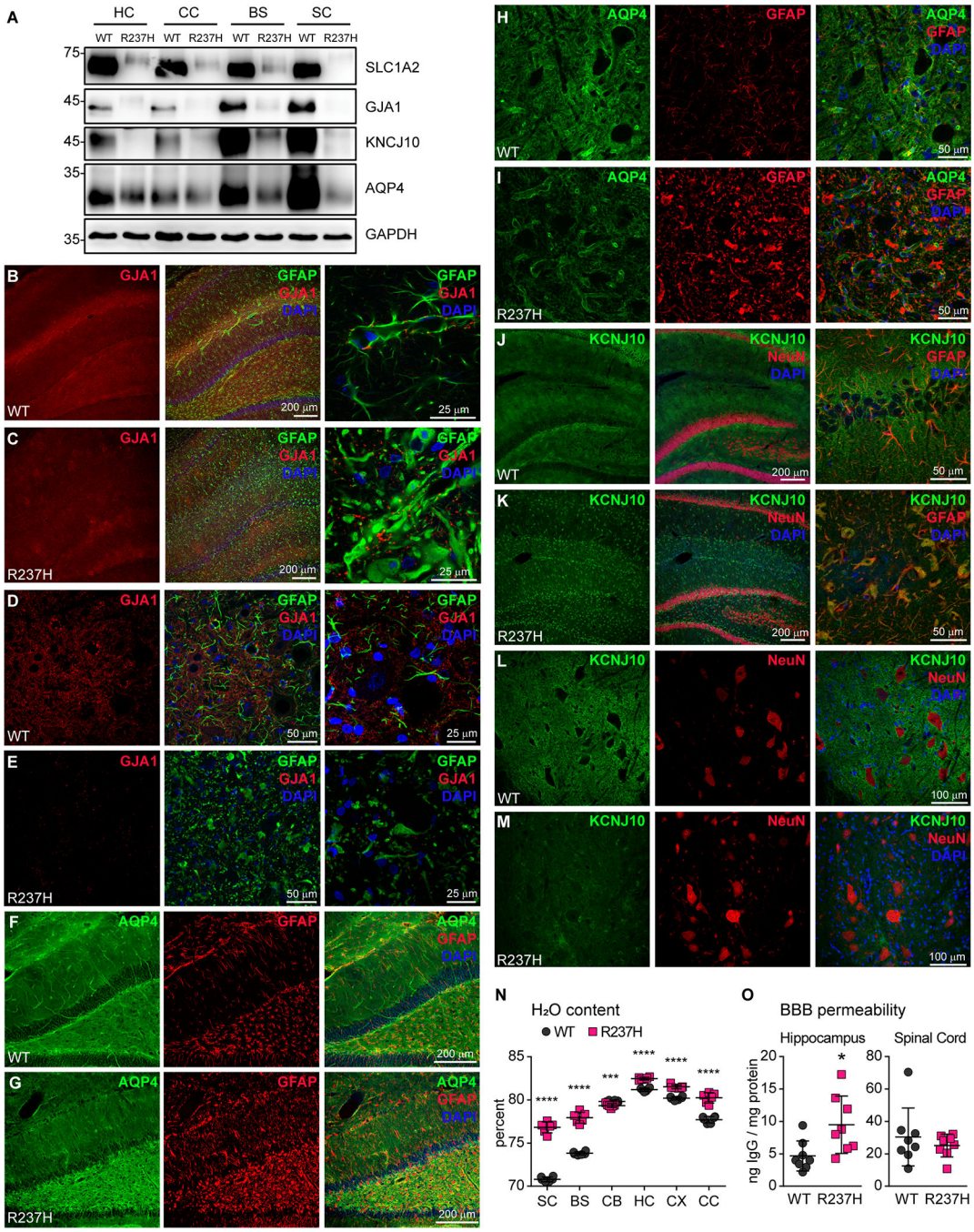

Fig. 4. Astrocyte function in R237H rats.

(**A**) Immunoblotting of membrane fractions from hippocampus (HC), corpus callosum (CC), brainstem (BS), and cervical spinal cord (SC) for proteins related to astrocyte function including glutamate transporter GLT1 (SLC1A2), connexin 43 (GJA1), aquaporin 4 (AQP4) and Kir4.1 (KCNJ10) in R237H rats compared with WT at 8 weeks of age [glyceraldehyde-3-phosphate dehydrogenase (GAPDH) loading control, N = 3, each with separate genotype pairs, representative blots shown]. (**B** to **E**) Immunofluorescence (IF) labeling of GJA1 and GFAP in hippocampus (**B** and **C**) and in spinal cord (cervical

ventral horn, **D** and **E**). DAPI, 4',6-diamidino-2-phenylindole. (**F** to **I**) AQP4- and GFAP-IF in hippocampus (**F** and **G**) and spinal cord (**H** and **I**; cervical ventral horn). (**J** to **M**) KCNJ10-IF in hippocampus (**J** and **K**; left panels show low magnification with NeuN labeling for orientation, and right panel shows higher magnification with GFAP colabel) and spinal cord gray matter (**L** and **M**). Confocal images are single optical slices, with the exception of higher magnification images in (**D**), (**E**), (**J**), and (**K**) (right panels), which are maximum projections. Camera and microscope settings were equivalent for comparisons between genotypes, n = 3 to 4 animals per genotype (males and females), and images are representative. (**N**) Comparison of percent water content in different CNS regions in R237H versus WT rats (***$P < 0.001$ and ****$P < 0.0001$, multiple *t* tests, Holm-Sidak correction method, $\alpha = 5\%$, n = 6 males). (**O**) Quantification of IgG content by ELISA to assess blood-brain barrier (BBB) integrity in saline-perfused female rats at 10 weeks of age in spinal cord and hippocampus (*$P < 0.05$, two-tailed *t* test, n = 8). All results from rats at 8 weeks except for (**O**). CB, cerebellum; CX, cortex.

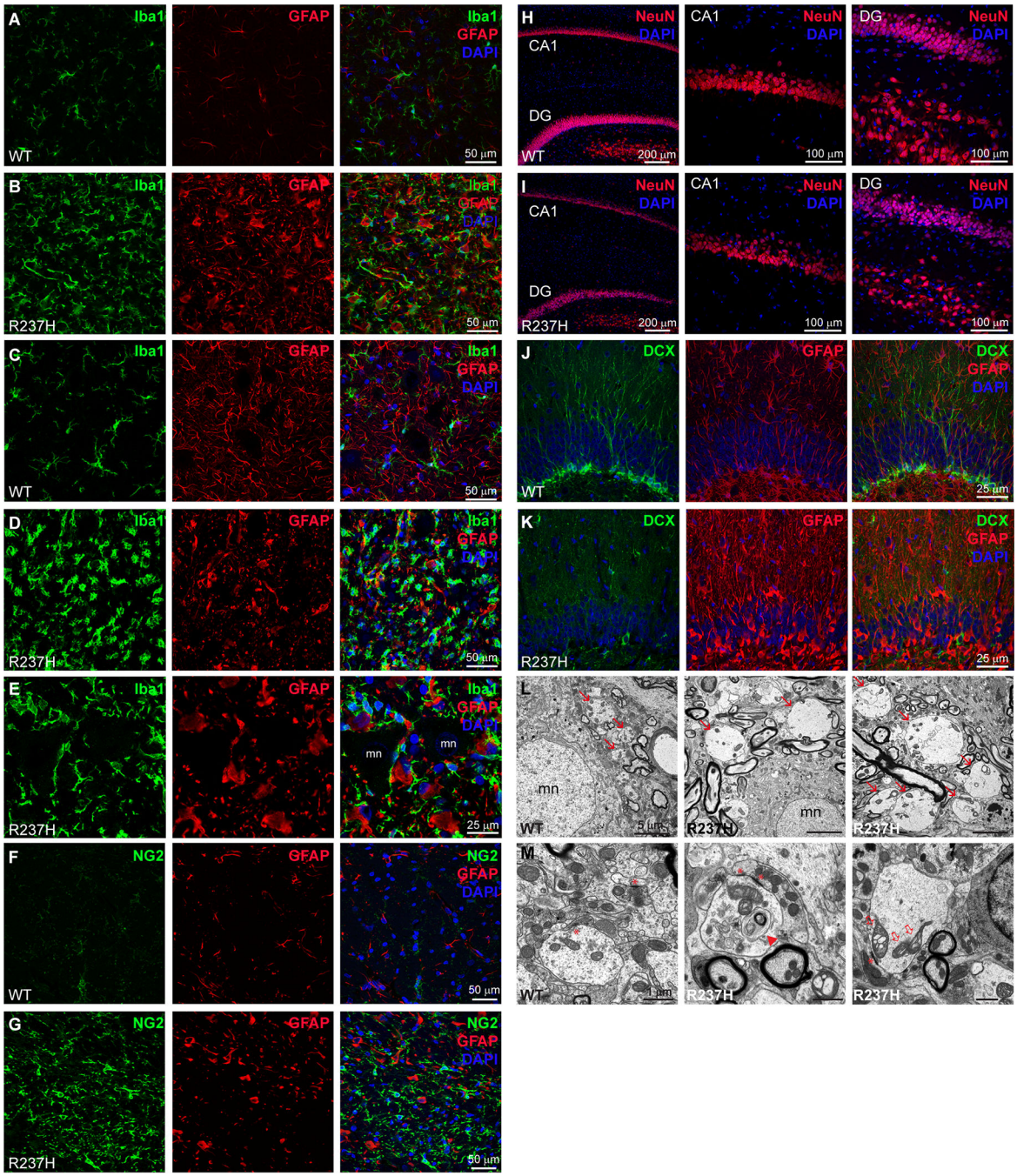

Fig. 5. Non-cell-autonomous effects of mutant GFAP and astrocyte dysfunction.

(**A** to **E**) Microglia identified by Iba1-IF labeling in R237H rats (**B**, **D**, and **E**) compared with WT (**A** and **C**) at 8 weeks of age in cortex (**A** and **B)** and cervical cord (**C** to **E**). mn, motoneuron. (**F** and **G**) NG2-IF labeling of oligodendrocyte precursor cells in corpus callosum. (**H** and **I**) NeuN-IF highlights pyramidal cells (CA1) and dentate granule cells (DG) in R237H versus WT rats. (**J** and **K**) Doublecortin (DCX) IF labeling of immature neurons in dentate gyrus in WT and R237H rats. (**L** and **M**) Electron microscopy in cervical cord ventral horn from R237H rats (left panel, WT; right two panels, R237H)

shows enlarged neurites (**L**; arrows), some of which show degeneration and collections of membranous debris (**M**; arrow head) and vacuolized mitochondria (open arrows). All animals at 8 weeks of age. Asterisks indicate synaptic densities. Scale bar, 5 μm in (**L**,), 1 μm in (**M**).

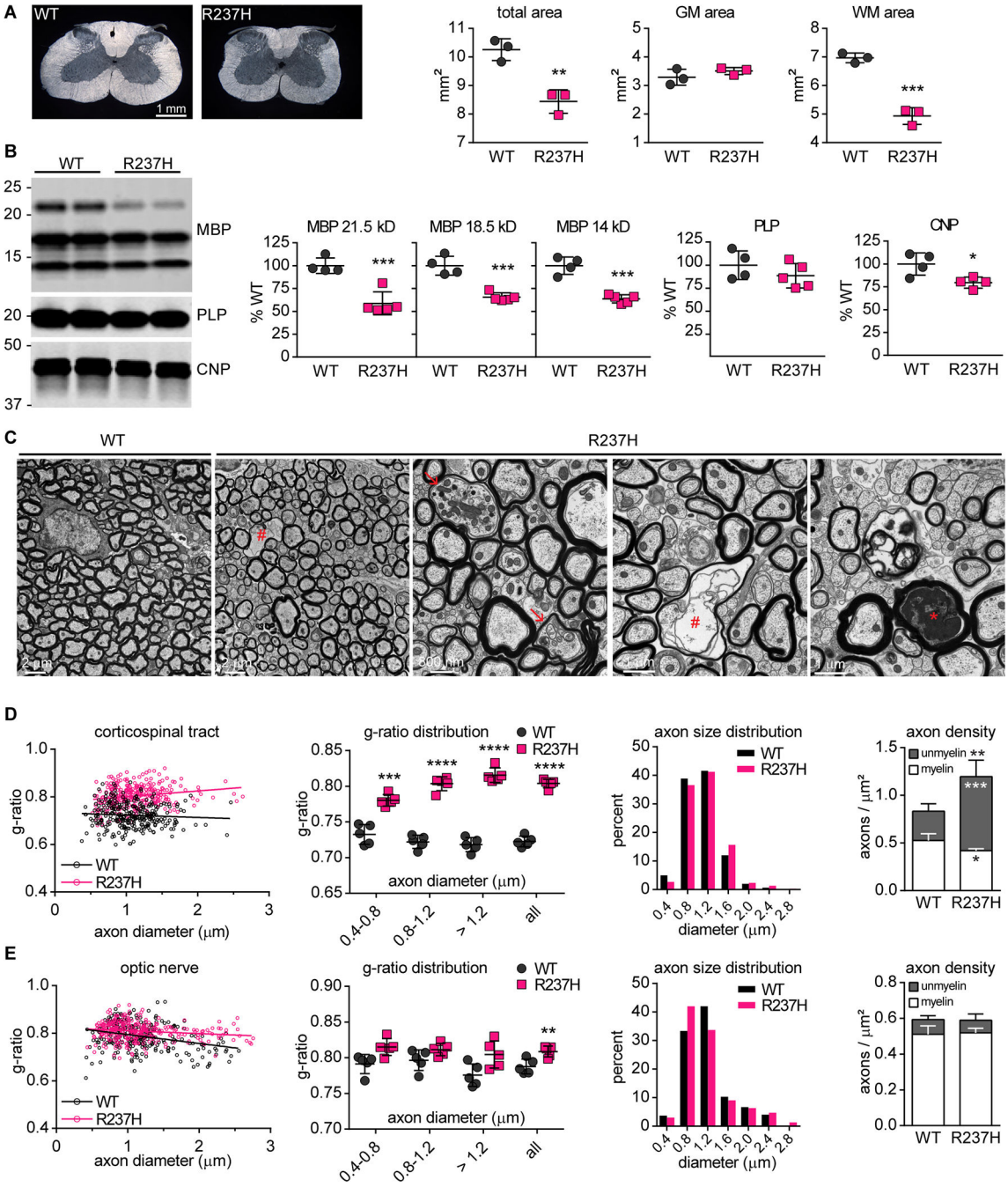

Fig. 6. Myelin deficits in R237H rat model of AxD.

(**A**) Area measures from cervical spinal cord cross sections at C5, including total area, white matter (WM), and gray matter (GM) at 8 weeks (two-tailed *t* test, males, n = 3). (**B**) Quantification of myelin proteins including MBP, CNPase, and PLP by western blot analysis of cervical cord protein homogenates (two-tailed *t* test, males and females at 8 weeks, n = 4 WT and n = 5 R237H for MBP and PLP, n = 4 for CNPase). (**C**) Electron microscopy shows thinning myelin and degenerating axons with accumulating organelles (arrows), dark cytoplasm (asterisk), and empty sheaths (hash symbol), in the dorsal corticospinal tract of

R237H rats. (**D**) Linear regression analysis of g-ratios in cervical spinal cord (panel 1; WT slope = −0.01000 ± 0.00848, R237H slope = 0.0237 ± 0.00727, $^{**}P = 0.00260$). Distribution of g-ratios for axons of different calibers, (panel 2; multiple *t* tests, Holm-Sidak correction method, $\alpha = 5\%$). Myelinated axon size distribution (panel 3, Kolmogorov-Smirnov test, $P = 0.520$). Quantification of unmyelinated and myelinated axon density (panel 4, multiple *t* tests as above). (**E**) Linear regression analysis of g-ratios in optic nerve (panel 1; WT slope = −0.0372 ± 0.00690, R237H slope = −0.0121 ± 0.00445, $^{**}P = 0.00193$) and g-ratios across axons of different calibers (panel 2, multiple *t* tests as above). Axon size distribution (panel 3, Kolmogorov-Smirnov test, $P = 0.121$). Quantification of unmyelinated and myelinated axon density (panel 4, multiple *t* tests as above). N = 5 males per genotype. For all tests: $^{*}P < 0.05$, $^{**}P < 0.01$, $^{***}P < 0.001$, $^{****}P < 0.0001$.

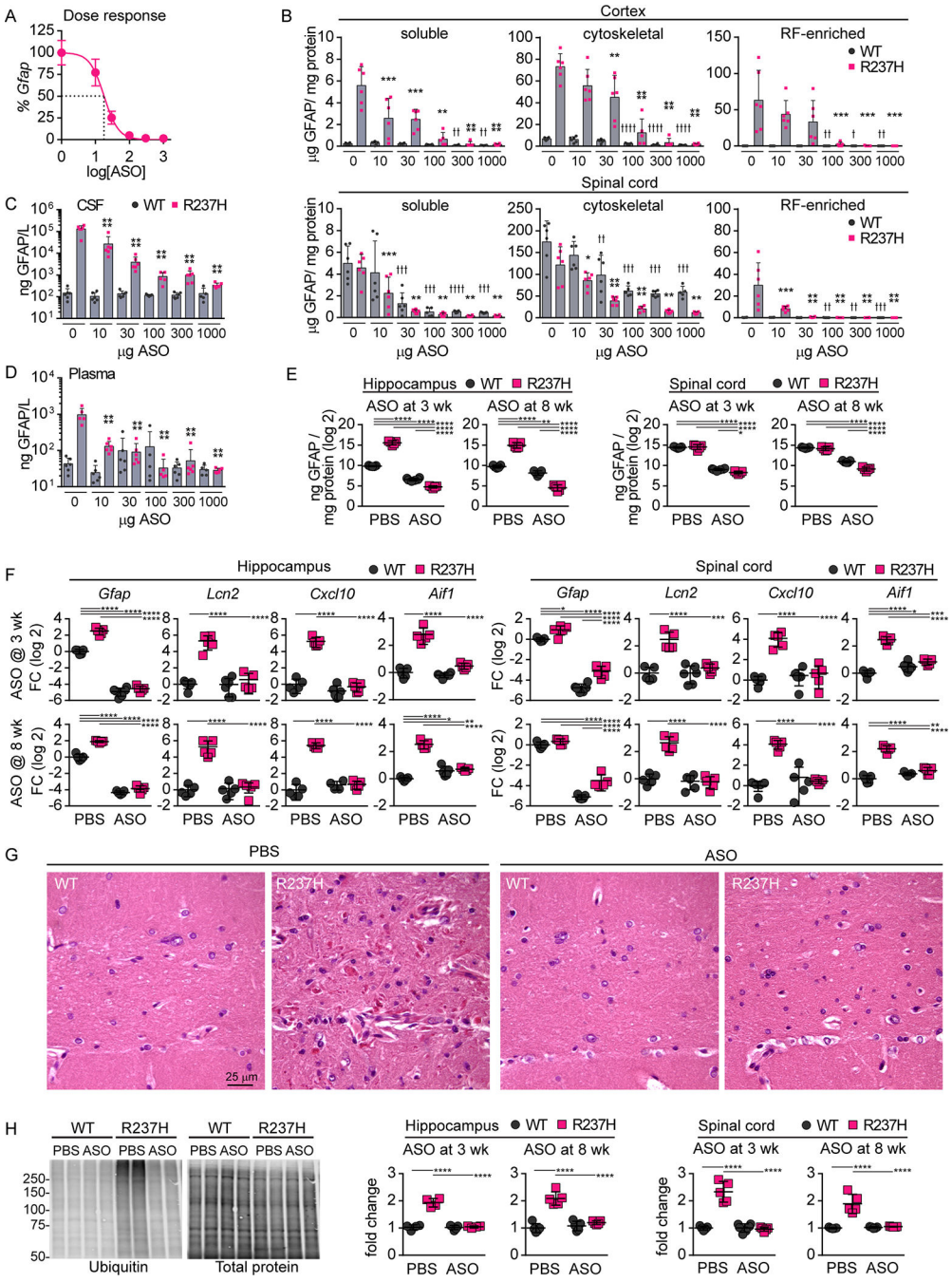

Fig. 7. GFAP suppression reverses AxD pathology.

(**A**) Dose response curve for increasing concentrations of *Gfap*-targeted ASO-5 (ICV), ranging from 10 to 1000 µg, and incremental reductions in *Gfap* transcript, as measured by qPCR in hippocampus from R237H rats, with a half-maximal effective concentration (EC50) of 18 µg (males and females treated at 10 weeks of age, tissues collected 8 weeks post-treatment, error = SEM). (**B** to **D**) Quantification of GFAP by ELISA in cortex and spinal cord protein fractions (**B**), CSF (**C**) and plasma (**D**) from the same cohort (one-way ANOVA comparisons to vehicle treated group within genotypes; * indicates R237H, and †

indicates WT for Dunnett's multiple comparisons test, n = 5 to 6). (**E**) Quantification of total GFAP in hippocampus and spinal cord from rats treated at 3 or 8 weeks of age with vehicle [phosphate-buffered saline (PBS)] or 300 μg of ASO for maximal *Gfap* suppression. (**F**) Transcript analysis (qPCR) of *Gfap* and other markers of astro- and microgliosis in rats treated at 3 weeks or 8 weeks (**E** and **F**; two-way ANOVA of log2-transformed values with Tukey's multiple comparisons, n = 5 except for WT rats treated at 3 weeks, n = 6). FC, fold change. (**G**) RF accumulation in PBS- versus ASO-treated rats (H&E stain, hippocampal stratum lacunosum moleculare shown from rats treated at 8 weeks). (**H**) Western blot analysis of high-molecular weight ubiquitinated proteins in hippocampus and spinal cord from R237H rats and WT controls treated at either 3 or 8 weeks. Western image shows representative hippocampal homogenates from rats treated at 8 weeks; left panel is ubiquitin, and right panel is total protein stain for normalization (two-way ANOVA with Tukey's multiple comparisons, n = 4 to 5 for hippocampus, n = 5 to 6 for spinal cord). For all post-test comparisons: */† $P < 0.05$, **/†† $P < 0.01$, ***/††† $P < 0.001$, and ****/†††† $P < 0.0001$.

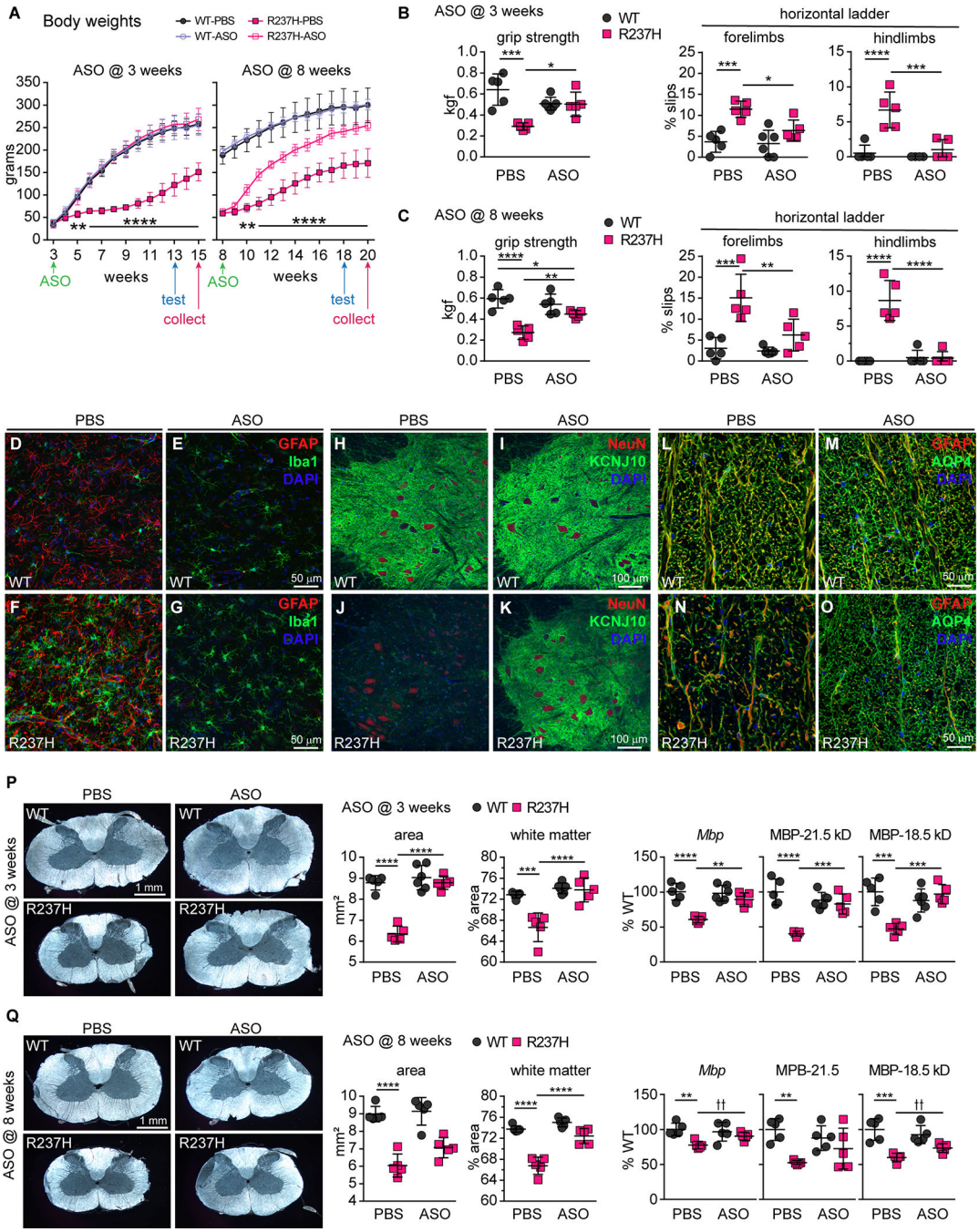

Fig. 8. GFAP suppression rescues motor deficits and AxD phenotypes.

(**A**) Body weights of rats receiving ASO compared with PBS vehicle at 3 or 8 weeks of age (females, repeated-measures two-way ANOVA, Bonferroni's multiple comparisons test, n = 5 except for WT rats treated at 3 weeks, n = 6). The timeline for treatment, behavior testing, and tissue collection is also noted. (**B** and **C**) Motor tests of forelimb grip strength [kilogram force (kgf)] and coordination with paw placement on the horizontal ladder in animals treated at 3 weeks (**B**) and at 8 weeks (**C**; 10 weeks after treatment, two-way ANOVA, Tukey's multiple comparisons test, n = 5 to 6). (**D** to **G**) Iba1 and GFAP immunofluorescence

labeling (IF) in cervical spinal cord gray matter (ventral horn) from R237H and WT rats treated at 8 weeks. (**H** to **O**) KCNJ10-IF (Kir4.1) in ventral horn gray matter (**H** to **K**), and AQP4-IF in white matter (**L** to **O**) of cervical cord from R237H and WT rats treated at 8 weeks. (**P** and **Q**) Area measures of cervical cord cross sections, including percent white matter, and quantification of MBP transcript and protein in rats treated at 3 weeks (**P**) and at 8 weeks (**Q**) (n = 5 to 6, *$P < 0.05$, **$P < 0.01$, ***$P < 0.001$, and ****$P < 0.0001$, *t* test for area measures, two-way ANOVA with Tukey's multiple comparisons tests for *Mbp* and MBP; †† $P < 0.01$, multiple t-tests within genotypes, Holm-Sidak correction method, α = 5%).